FULL PAPER

Electronic Skin

**ADVANCED
FUNCTIONAL
MATERIALS**

www.afm-journal.de

Self-Powered Noncontact Electronic Skin for Motion Sensing

Hanxiang Wu, Zongming Su, Mayue Shi, Liming Miao, Yu Song, Haotian Chen, Mengdi Han, and Haixia Zhang*

The advancement of electronic skin envisions novel multifunctional human machine interfaces. Although motion sensing by detecting contact locations is popular and widely used in state-of-the-art flexible electronics, noncontact localization exerts fascinations with unique interacting experiences. This paper presents a self-powered noncontact electronic skin capable of detecting the motion of a surface electrified object across the plane parallel to that of the electronic skin based on electrostatic induction and triboelectric effects. The displacement of the object is calculated under the system of polar coordinates, with a resolution of 1.5 mm in the lengthwise direction and 0.76° in the angular direction. It can serve as a human machine interface due to its ability to sense noncontact motions. An additional self-powered feature, enabled by its physical principles, solves the problem of power supply. This electronic skin consists of trilayers of polyethyleneterephthalate–indium tin oxide–polydimethylsiloxane (PDMS) films, and microstructured PDMS as the electrified layer, which can be achieved through simplified, low cost, and scalable fabrication. Transparency, flexibility, and less number of electrodes enable such electronic skin to be easily integrated into portable electronic devices, such as laptops, smart phones, healthcare devices, etc.

1. Introduction

Electronic skins are drawing more and more attentions in recent years due to their nature of wearable electronics and the potential to integrate a variety of sensing capabilities,[1,2] such as force[3,4,30] (including pressure,[5–7] strain,[8] bending,[9] torsion, and shear[10]), humidity,[11] temperature,[12] motion,[13,14] and chemicals,[15] just like the skins do. Among all these functions, motion sensing is one of the most important one for artificial intelligences, because motion is a simple

and efficient way for humans to interact with them. Most electronic skins rely on contact localization for motion sensing, and there are various ways to realize it. Piezoresistive,[16,17] capacitive,[18] active devices,[19–22] etc., are applied to fabricate the contact sensing units, and the array of such units forms the localizing sensor. However, major drawbacks exist in power consumption and resolution. Frequent recharge of batteries is unavoidable for the former ones; resolution enhancement relies on increased number of sensing units which leads to huge number of electrodes in the latter ones. Both of the disadvantages severely hamper the feasibility of a portable electronic system featuring electronic skins. Nevertheless, self-powered systems[23–31] and localizing methods based on ratios of electrode voltages[32,33] point out potential solutions. The former ones harness the energy in the surrounding environment and thus provide the opportunity to get rid of batteries, while the latter ones can achieve a theoretical resolution of infinity with low number of electrodes.

All electronic skins relying on contact localization encounter the problem of long term reliability, since abrasion is inevitable. More than ever, it confines the possibility and versatility of motions, that is, only limited kinds of motions, such as touching and sliding can be detected. The interaction between human and computer can become more efficient and captivating if given more freedom to the motion of human. As a result, an electronic skin with noncontact motion sensing method is promising in potential applications, e.g., integrating into screens of smartphones, because it freed the users from the necessity of touching. Instead, this enables the users' fingers to roam above the interface, while numerous kinds of motions can be perceived.

Herein, a self-powered noncontact electronic skin based on electrostatic induction and triboelectric effects is presented, which is capable of detecting motions of an object with enough surface electrification. Voltage waveforms are acquired from the four electrodes; ratios of peak voltages are then calculated to determine the displacement of the object, which is in plane parallel to that of the electronic skin, under the system of polar coordinates. Polyethyleneterephthalate (PET)–indium

H. Wu, Dr. Z. Su, Dr. M. Shi, Dr. L. Miao, Dr. Y. Song,
Dr. M. Han, Prof. H. Zhang
National Key Laboratory of Science and Technology
on Micro/Nano Fabrication
Peking University
Beijing 100871, China
E-mail: zhang-alice@pku.edu.cn
Dr. H. Chen, Prof. H. Zhang
Academy for Advanced Interdisciplinary Studies
Peking University
Beijing 100871, China

1704641 (1 of 10)

tin oxide (ITO) film is fabricated by magnetron sputtering and laser patterning, in which PET film serves as the transparent substrate and patterned ITO forms the quarter annulus transparent electrodes, while another thin layer of patterned flat polydimethylsiloxane (PDMS) is covered on the PET–ITO film to promote its durability. In addition, microstructured PDMS film is used as the electrified layer to be attached on moving objects. Localizing method based on ratios of electrode voltages greatly reduced the number of electrodes, and in this case to four. Moreover, the triboelectric mechanism enables the device to be self-powered. Furthermore, noncontact motion sensing is the main highlight point of this work, since spatial electrostatic induction introduces a new degree of freedom to the interaction between human and artificial intelligence.

2. Results and Discussions

The structure diagram of the electronic skin and its entity are demonstrated in **Figure 1**a,b, respectively. The inset image is a microstructured PDMS film attached to a cotton finger-cot. A thin layer of ITO with a sheet resistance of 35 Ω sq^{-1} was deposited on a PET film by magnetron sputtering, and then patterned by laser corrosion. PET film serves as the transparent substrate, while conducting ITO forms the transparent electrodes. As Figure S1a (Supporting Information) shows, the shape of each electrode is quartered annulus, with an outer radius of 4 cm and an inner radius of 3.5 cm. The separation between the two closest edges of adjacent electrodes is 1 cm. A patterned flat PDMS film was placed on the PET–ITO film to promote the durability of the device. The purpose of the hollow
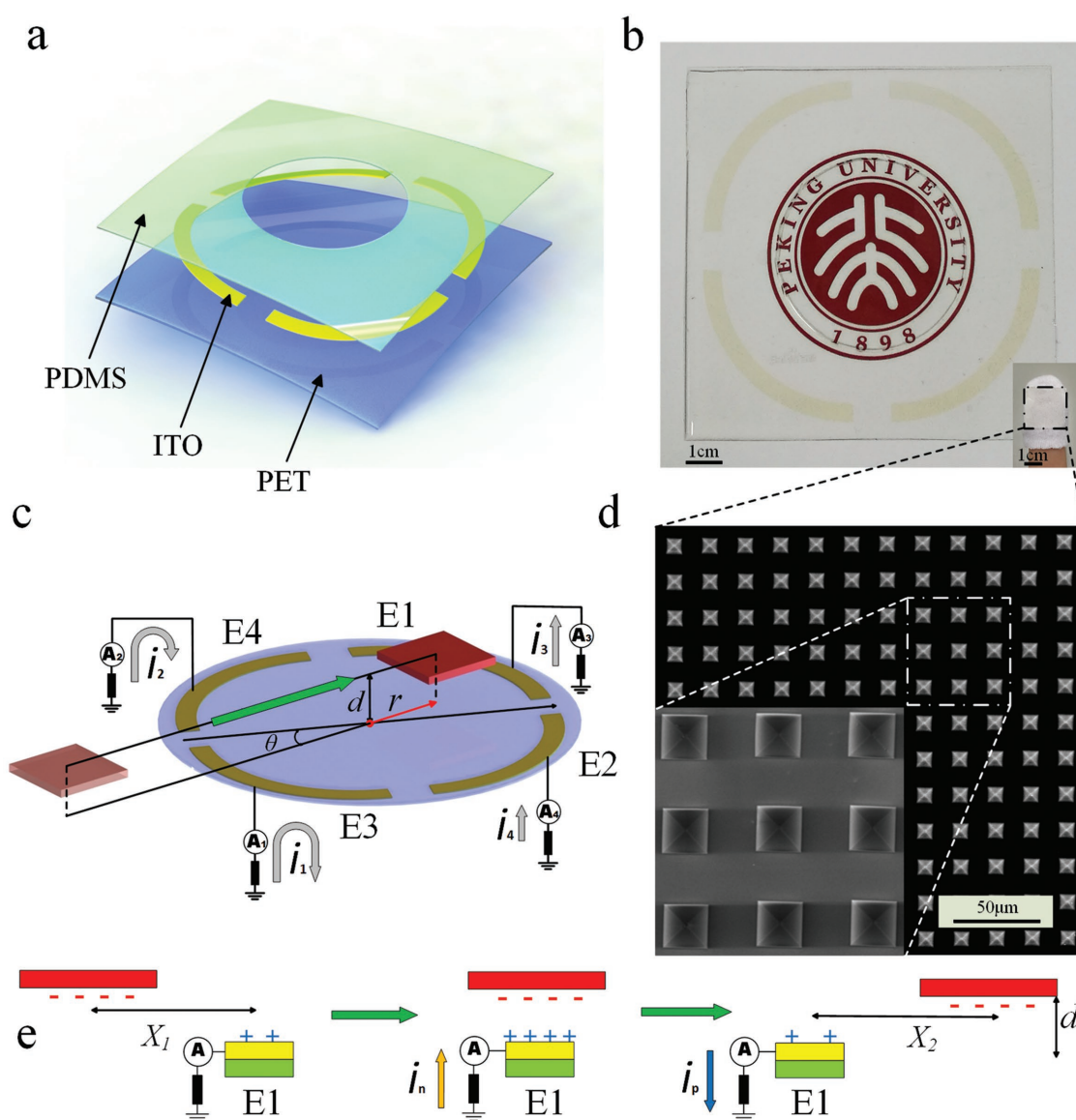
Figure 1. Structure and illustration of the working principle of noncontact electronic skin. a) Schematic diagram of a noncontact electronic skin. b) The optical image of the transparent and flexible electronic skin. c) Illustration of the working principle of the electronic skin. d) SEM image of microstructures on the PDMS film. e) Schematics of working mechanism of single electrode electronic skin.

area in the center of the PDMS film is to expose a PET friction layer to contact with the microstructured PDMS attached on moving objects. The electrodes are design in such configurations because symmetry is desired and annuluses maximize the effective region given the same area. The electronic skin is thus flexible and transparent, with an average transmittance of 88% (see Figure S1d, Supporting Information). The PDMS for the surfaced electrified object is microstructured with pyramid array using a Si mold. The microstructure is fabricated to enhance the surface area and thus promotes the amount of surface charge. With increased surface charge, the output voltage as well as the signal-noise ratio will be improved.[34] The working principle of the electronic skin is shown in Figure 1c. Scanning electron microscope (SEM) image of the PDMS microstructure is shown in Figure 1d, and the fabrication process can be referred in the Experimental Section.

In the beginning of a cycle, several intervals of contact and separation are performed by the moving object against the exposed PET film to accumulate triboelectric charges. The size of the object is a square with a length of 2 cm. As a result, the PDMS layer attached to the bottom surface of the object is negatively charged due to triboelectric effects and the strong ability of PDMS to attract electrons. After the contact and separation process, the object is surfaced electrified and capable of completing multiple cycles without contacting with the electronic skin before another process is needed to supplement the surface charge. Afterwards, the object moves in a straight line, and two sides of the square are parallel to the moving direction while the other two are perpendicular to it. The bottom surface is inside the plane parallel to that of the electronic skin, and the coincidence between projections of trajectory of the center of the square object and the center of the electronic skin is required. The two key factors that the electronic skin can determine are the distance r (0 cm $< r \leq 4$ cm) between the center of the electronic skin and projections of the stop point of the object center, and the moving direction θ ($0° \leq \theta < 45°$). θ is defined as the angle between the displacement vector $\vec{r}$ and the symmetry axis of the electronic skin which separates two adjacent electrodes from the other two. The cycle begins when the projections of the object is out of the electronic skin, and ends when the object is stopped with its projections inside the electronic skin, which is approximately a circle with a radius of 4.5 cm. As is shown in Figure 1c, four electrodes receive different voltages during one cycle of operation. Two of the electrode–object distances experienced decrease followed by increase (corresponds to E3 and E4), while the other two only decreased but not increased (corresponds to E1 and E2). According to electrostatics, the absolute value of electrode's potential will increase when the charged object is moving toward it, and decrease with it is moving away from it. And when the distance between object and electrode decreases, positive charges are attracted to the electrode due to electrostatic induction; positive charges is driven away from it when the distance increases. Figure 1e illustrated this mechanism by showing the schematic of a single electrode electronic skin including charge moving. The open circuit peak voltages of the electrode are directly proportional to the change of electric potential during the two phases: distance decrease and then increase. Since the resistances of the oscilloscope's probes are 100 MΩ, which is far greater than the

sheet resistance of the ITO electrode which is 35 Ω sq^{-1}, the voltages obtained by the oscilloscope can be taken as open circuit voltages. The electric potential of the electrode imposed by a surface charge of the moving object is set as $U_{S_i}(r, \theta)$, where (r, θ) are the coordinates of the center of the square object and i is the number of electrodes corresponding to Figure 1c. Hence, the absolute voltages from all the four electrodes can be given as follows

$$V_{n_i} = \alpha \left[U_{S_i}(r_1, \theta_1) - U_{S_i}(r_2, \theta_2) \right] (r_2 < r_{m_i}) \tag{1}$$

$$V_{n_i} = \alpha \left[U_{S_i}(r_1, \theta_1) - U_{S_{i\max}}(r_{m_i}, \theta_{m_i}) \right] (r_2 \geq r_{m_i}) \tag{2}$$

$$V_{p_i} = 0 (r_2 < r_{m_i}) \tag{3}$$

$$V_{p_i} = \alpha \left[U_{S_i}(r_2, \theta_2) - U_{S_{i\max}}(r_{m_i}, \theta_{m_i}) \right] (r_2 \geq r_{m_i}) \tag{4}$$

Where v_{n_i} corresponds to the negative peak voltage and v_{p_i} stands for the positive peak voltage. (r_1, θ_1) correspond to the coordinates of the start point and (r_2, θ_2) correspond to the stop point. (r_{m_i}, θ_{m_i}) are the coordinates when maximum electrostatic voltage is obtained on electrode no. i respectively, and is determined by (r_1, θ_1) and (r_2, θ_2). α is the scale coefficient, which is directly proportional to the charge density of the moving object and will be reduced in the following calculations, since the results only rely on voltage ratios. Because the negative peak voltage of E3 is the biggest one, it is chosen to be the normalization factor, i.e., all peak voltages are divided by it. As mentioned before, the result is irrelevant to the amount of charges on the object, and the peak voltages mentioned afterwards mean normalized voltages unless stated otherwise. In practice, the positive peak voltage of E3 and the negative voltages of E2 and E4 were found out to remain relatively constant despite the change in r or θ and are thus noncontributing to the calculations. So there are only three peak voltages that can be used in the calculations, including the one that is used as the normalization factor. The two parameters

$$R_r = \frac{v_{n_1}}{v_{n_3}} = \frac{U_{S_1}(r_1, \theta_1) - U_{S_1}(r_2, \theta_2)}{U_{S_3}(r_1, \theta_1) - U_{S_3\max}(r_{m_3}, \theta_{m_3})} \tag{5}$$

$$R_\theta = \frac{V_{p_4}}{V_{n_3}} = \frac{U_{S_4}(r_2, \theta_2) - U_{S_4\max}(r_{m_4}, \theta_{m_4})}{U_{S_3}(r_1, \theta_1) - U_{S_3\max}(r_{m_3}, \theta_{m_3})} \tag{6}$$

are to solve the unknown r and θ. Because there are three symmetry axes in the electronic skin, only $\frac{1}{2^3} \times 360° = \frac{1}{8} \times 360° = 45°$ of θ is demonstrated in our work. **Figure 2**a–d demonstrated the voltage waveforms with three different cases of (r, θ). The restriction of r and θ is $r_1 \leftarrow 4$ cm, $r_2 > 0$ cm, and $r_2 \leq 4$ cm with $\theta \geq 0°$ and $\theta < 45°$.

Figure 3a displayed the working principle of a double-electrode electronic skin including charge moving, in which $\theta = 0$ and its structure diagram is shown in Figure S1b (Supporting Information). Figure 3b–d are the simulation results of the output peak voltage ratio of it. Figure 3b illustrates the effect of

**ADVANCED
SCIENCE NEWS**
www.advancedsciencenews.com

**ADVANCED
FUNCTIONAL
MATERIALS**
www.afm-journal.de
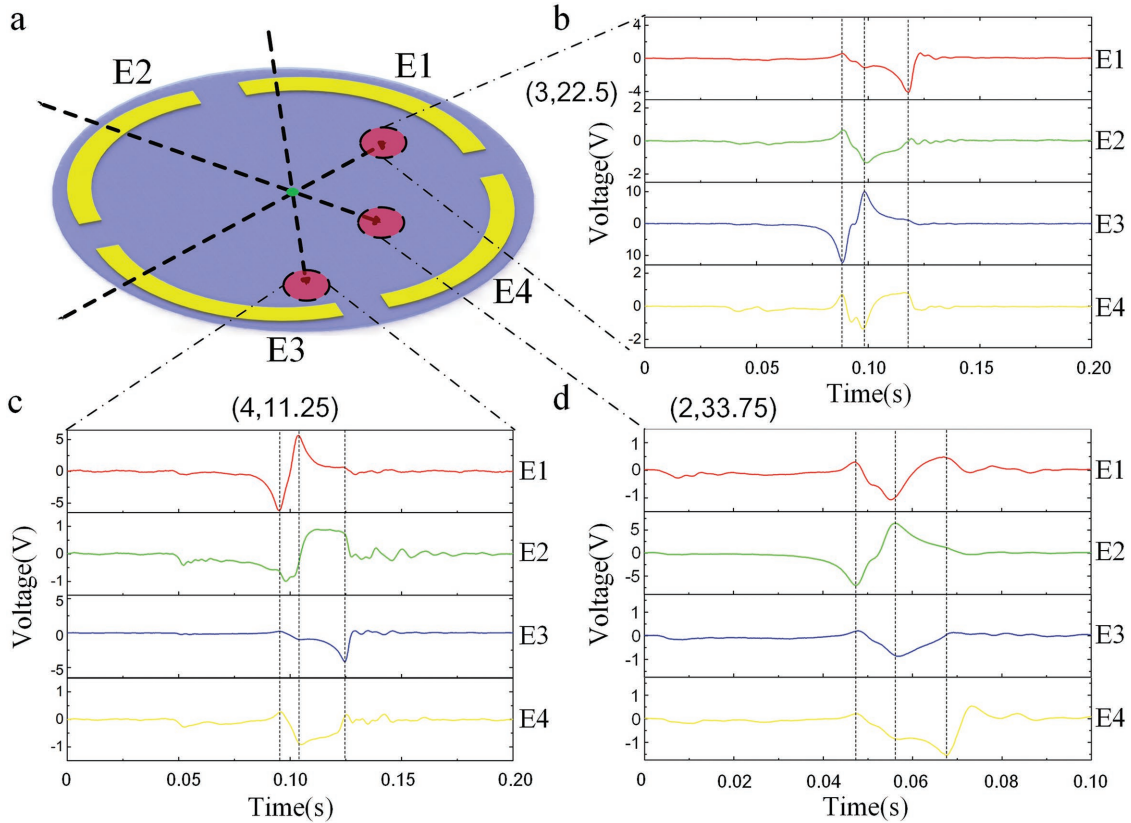
Figure 2. Working principle of electronic skin. a) Three instances of voltage waveforms corresponding to three different polar coordinates of the stop point. The first coordinate is r, with a unit of cm; the second one is θ, with a unit of degree. b) Voltage waveforms from four electrodes triggered by motion of a 2 cm × 2 cm square object with the coordinates of stop point as (3 cm, 22.5°). c) Voltage waveforms from four electrodes triggered by motion of the object with coordinates of stop point as (4 cm, 11.25°). d) Voltage waveforms from four electrodes triggered by motion of the object with the coordinates of stop point as (2 cm, 33.75°).

x_1 and d in the ratio of E1's negative peak voltage over its fixed positive peak voltage, i.e., fixed $x_{20} = 50$ mm (variables and electrode numbers marked in Figure 3a). The function of the curve in Figure 3b is

$$R_{n_1 p_1} = \frac{U_{S_1}(x_1) - U_{S_1 \max}(x_m)}{U_{S_1}(x_2) - U_{S_1 \max}(x_m)}(x_m = 0) \tag{7}$$

With a point charge simplification, which considers the cuboid electrode and the charged surface as particles, the expression of the voltage ratio can be calculated as

$$R_{n_1 p_1} = \frac{\dfrac{1}{d} - \dfrac{1}{\sqrt{d^2 + x_1^2}}}{\dfrac{1}{d} - \dfrac{1}{\sqrt{d^2 + x_{20}^2}}} = \frac{1 - \dfrac{1}{\sqrt{1 + \dfrac{x_1^2}{d^2}}}}{1 - \dfrac{1}{\sqrt{1 + \dfrac{x_{20}^2}{d^2}}}} \tag{8}$$

It is obvious that $R_{n_1 p_1}$ is a monotone increase function of x_1, with a second derivative first increase and then decrease. When d decreases from 20 to 2.5 mm, $R_{n_1 p_1}$ achieves a stable value near 1 more swiftly, i.e., with a smaller value of x_1. And $R_{n_1 p_1}$ is insensitive to a further increase in x_1. As a result,

negative peak voltage of the normalization electrode is stable with d small enough and x_1 big enough, so that it is suitable for being the normalization factor. And this is also the reason that positive peak voltage of E3 and negative peak voltages of E2 and E4 remain constant. Function $R_{n_1 p_1}$ with different d intersects at 1 when $x_1 = 50$ mm because $x_{20} = 50$ mm is used as the reference, while its selection does not affect the conclusion. In summary, R_r and R_θ can be simplified into

$$R_r = \frac{v_{n_1}}{v_{n_3}} = \frac{U_{S_1}(r_1, \theta_1) - U_{S_1}(r_2, \theta_2)}{-U_{S_3 \max}(r_{m_3}, \theta_{m_3})} \tag{9}$$

$$R_\theta = \frac{V_{p_4}}{V_{n_3}} = \frac{U_{S_4}(r_2, \theta_2) - U_{S_4 \max}(r_{m_4}, \theta_{m_4})}{-U_{S_3 \max}(r_{m_3}, \theta_{m_3})} \tag{10}$$

The curves in Figure 3c illustrate the effect of x_2 and d in the ratio of E1's positive peak voltage over its fixed negative peak voltage, i.e., fixed $x_{10} = 50$ mm (variables and electrode numbers marked in Figure 3a), and can be expressed as

$$R_{p_1 n_1} = \frac{U_{S_1}(x_2) - U_{S_1 \max}(x_m)}{U_{S_1}(x_1) - U_{S_1 \max}(x_m)} = \frac{U_{S_1}(x_2) - U_{S_1 \max}(x_m)}{-U_{S_1 \max}(x_m)}(x_m = 0) \tag{11}$$

ADVANCED
SCIENCE NEWS
www.advancedsciencenews.com

ADVANCED
FUNCTIONAL
MATERIALS
www.afm-journal.de
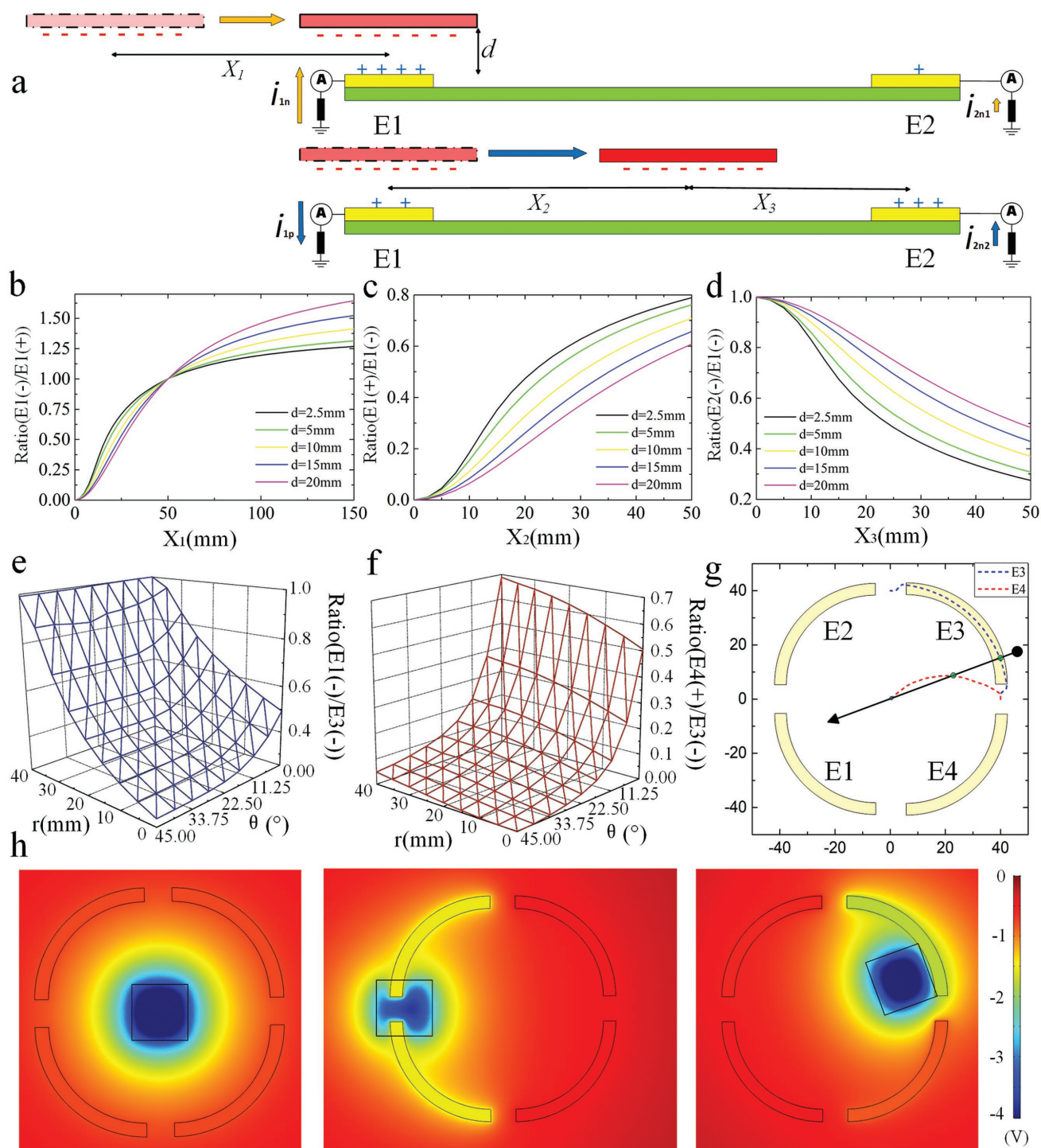
Figure 3. Simulation result of single-electrode electronic skin and four-electrode electronic skin using COMSOL (COMSOL Inc., USA). a) Illustrations of working mechanism of a double-electrode electronic skin. b) Effect of x_1 and d in the ratio of E1's negative peak voltage over its fixed positive peak voltage. c) Effect of x_2 and d in the ratio of E1's positive peak voltage over its fixed negative peak voltage. d) Effect of x_3 and d in the ratio of E2's negative peak voltage over E1's fixed negative peak voltage. e) Distribution of R_r in the polar coordinate system. f) Distribution of R_θ in the polar coordinate system. g) Collection of the projections of points where the absolute values of electrostatic voltages of E3 and E4 reached their maximum respectively, with θ changing from 0° to 45° (curves of E3 with θ from 45° to 90° is also shown to display its symmetry). h) Electrostatic potential distributions with different charge locations.

**ADVANCED
SCIENCE NEWS**
www.advancedsciencenews.com

**ADVANCED
FUNCTIONAL
MATERIALS**
www.afm-journal.de

Identically with a point charge simplification, the expression of the voltage ratio is

$$
R_{p_1 n_1} = \frac{\dfrac{1}{d} - \dfrac{1}{\sqrt{d^2 + x_2^2}}}{\dfrac{1}{d} - \dfrac{1}{\sqrt{d^2 + x_{10}^2}}} = \frac{1 - \dfrac{1}{\sqrt{1 + \dfrac{x_2^2}{d^2}}}}{1 - \dfrac{1}{\sqrt{1 + \dfrac{x_{10}^2}{d^2}}}} = 1 - \frac{1}{\sqrt{1 + \dfrac{x_2^2}{d^2}}}
\tag{12}
$$

It can be found out that with an increasing d, $R_{p_1 n_1}$ decreases while its linearity elevated, which means saturation of $R_{p_1 n_1}$ will be achieved at larger x_2.

The curves in Figure 3d illustrate the effect of x_3 and d in the ratio of E2's negative peak voltage over E1's fixed negative peak voltage, i.e., fixed $x_{10} = 50$ mm (variables and electrode numbers marked in Figure 3a), and can be expressed as

$$
R_{n_2 n_1} = \frac{U_{S_2}(x_1 + 100) - U_{S_2}(x_3)}{U_{S_1}(x_1) - U_{S_1 max}(x_{m_1})} = \frac{U_{S_2}(x_1 + 100) - U_{S_2}(x_3)}{-U_{S_1 max}(x_{m_1})} (x_{m_1} = 0)
\tag{13}
$$

Analytical expression with point charge simplification of the voltage ratio

$$
R_{n_2 n_1} = \frac{\dfrac{1}{\sqrt{d^2 + x_3^2}} - \dfrac{1}{\sqrt{d^2 + (x_{10} + 100)^2}}}{\dfrac{1}{d} - \dfrac{1}{\sqrt{d^2 + x_{10}^2}}} = \frac{1}{\sqrt{1 + \dfrac{x_3^2}{d^2}}}
\tag{14}
$$

Note that $x_2 + x_3 = 100$ mm. It is a monotone decrease function of x_3, while saturation is achieved with larger x_3 (this time its value close to 0) when d increases. Hence $R_{n_2 n_1}$ is larger when d increases.

Figure 3e,f shows the simulation result of R_r and R_θ of the four-electrode electronic skin, respectively. Figure 3g demonstrated the projection of the minimum distance point between E3 and E4 with the center of the object when θ changes. R_r and R_θ have good monotonicity with r and θ, which is essential to motion localization. It can be seen from Figure 3e that $\dfrac{\partial R_r(r, \theta)}{\partial \theta} < 0$ except when ≈ 20 mm $< r < 40$ mm and $\theta > 22.5°$. $\dfrac{\partial R_r(r, \theta)}{\partial \theta} < 0$ because larger θ results in smaller θ direction deviation from the equivalent center of E1 (electrode numbers marked in Figure 1c), which is apparently at $\theta = 45°$ due to symmetry. And a smaller θ direction deviation leads to smaller distance to the equivalent center, which corresponds to smaller d in Figure 3d, namely larger V_{n_3} and smaller R_r values. While in regions that $\dfrac{\partial R_r(r, \theta)}{\partial \theta} > 0$, it is because the r coordinate of the electrode equivalent center decreases with an increasing θ, resulting in a decrease in r coordinates of the minimum distant points corresponding to the blue dashed line in Figure 3g. That means V_{n_1} can achieve larger value with the same r coordinate than other θ values, causing R_r to be larger and $\dfrac{\partial R_r(r, \theta)}{\partial \theta} > 0$.

This is also in accord with the curves demonstrated in Figure 3d. $\dfrac{\partial R_\theta(r, \theta)}{\partial \theta} < 0$ is presented in Figure 3f but this time with drastic change along θ direction. It is caused by a larger θ direction deviation from the equivalent center of E4 (electrode numbers marked in Figure 1c) when θ increases. Meanwhile, the linearity along the r direction increases, because increased θ direction deviation equals to larger d value in Figure 3c.

With the distribution of R_r and R_θ along r and θ directions, the coordinate of the stop point of arbitrary motions can be calculated, e.g., (a, b) through intersections of R_r and R_θ by planes of $R_r(r, \theta) = R_r(a, b)$ and $R_\theta(r, \theta) = R_\theta(a, b)$, corresponding to the acquired voltage ratio, respectively. After projecting the two results which are implicit functions $r_1(\theta)|_{R_r(r, \theta) = R_r(a, b)}$ and $r_2(\theta)|_{R_\theta(r, \theta) = R_\theta(a, b)}$, the intersection point is acquired, which corresponds to the stop point of the motion and is considered as the experiment result. Figure 3h shows the electrostatic voltage distributions with different charge locations using a finite element analysis. It demonstrated the pattern of electrostatic potential distribution when equipotential bodies exist.

Figure 2a–d illustrated the effect of secondary induced charge flow which is not taken into account by the simulation model. For naming issues, besides the electrode which has the largest absolute peak voltage that was named the normalization electrode, r-sensitive electrode was adopted to refer to the one which is opposite to the normalization electrode, and θ-sensitive electrode to refer to the one which is on the same side with the starting point (r_1, θ_1) of the $\theta = 0°$ line. In the consequence of normalization, r-sensitive, θ-sensitive electrodes, they are E3, E1, and E4 in Figure 2b; E1, E3, and E2 in Figure 2c; and E2, E4, and E1 in Figure 2d. Vertical lines matching the largest three peaks in a single cycle are shown in the waveforms, which correspond to the positive and negative peaks of normalization electrode and the negative voltage of the r-sensitive electrode. When the normalization electrode reached the maximum negative peak voltage, positive peaks emerge in all other three electrodes. This can only be explained as the effect of secondary induced charges, because the distances between the moving object and other three electrodes did not increase. Namely, negative voltage change of normalization electrode caused positive charge flow in itself, and this in turn caused negative charge flows in other three electrodes, which simultaneously led to smaller positive peaks superimposed in the respective waveforms. It can be estimated that the original negative peak voltage is 10 times larger than the peak voltages caused by secondary induced charges. Identically, the positive peak voltage of normalization electrode is achieved simultaneously with negative peak voltages in other three electrodes. This slightly weakened the positive peak voltage of θ-sensitive electrode, while slightly enhanced the negative peak voltage of r-sensitive electrode. At last, the negative peak voltage in r-sensitive electrode caused secondary induced voltage in θ-sensitive electrode. Interestingly, this effect becomes more prominent with θ increasing, because the time difference between negative peak voltage of r-sensitive electrode and positive peak voltage of θ-sensitive electrode decreases, which promoted the superimposed positive voltage in θ-sensitive electrode. However, it can be seen that the voltage value of θ-sensitive electrode when maximum value is achieved in r-sensitive electrode

ADVANCED
SCIENCE NEWS
www.advancedsciencenews.com

ADVANCED
FUNCTIONAL
MATERIALS
www.afm-journal.de

is only slightly larger than the voltage representing the distance increase between the θ-sensitive electrode and the object, which is weakened by the charge flow in normalization electrode. As a result, the voltage of θ-sensitive electrode in fact has no prominent change comparing with the simulation result. Since the time deviations between the peak of causal electrode and both the r-sensitive and θ-sensitive electrodes are greater than the full width at half maximum (FWHM) of the former, plus the secondary induced peak voltage is approximately 10 times smaller than the causal peak voltage, the secondary induced effect will not notably affect the peak voltage of r-sensitive and

θ-sensitive electrodes, and thus will not alter the conclusions acquired with the simulation results. In addition, we have developed specific algorithm to distinguish the waveforms acquired in four channels, and thus discriminate the normalization electrode, r-sensitive electrode, and θ-sensitive electrode regardless of the coupling effect. Detailed information can be found in Note 1.2 (Supporting Information).

Figure 4a–c shows the testing results of double-electrode electronic skin (diagram shown in Figure 3a) with $d = 2.5$ mm corresponding to voltage ratios elucidated in Figure 3b–d, respectively. It can be seen that the testing results are in accord
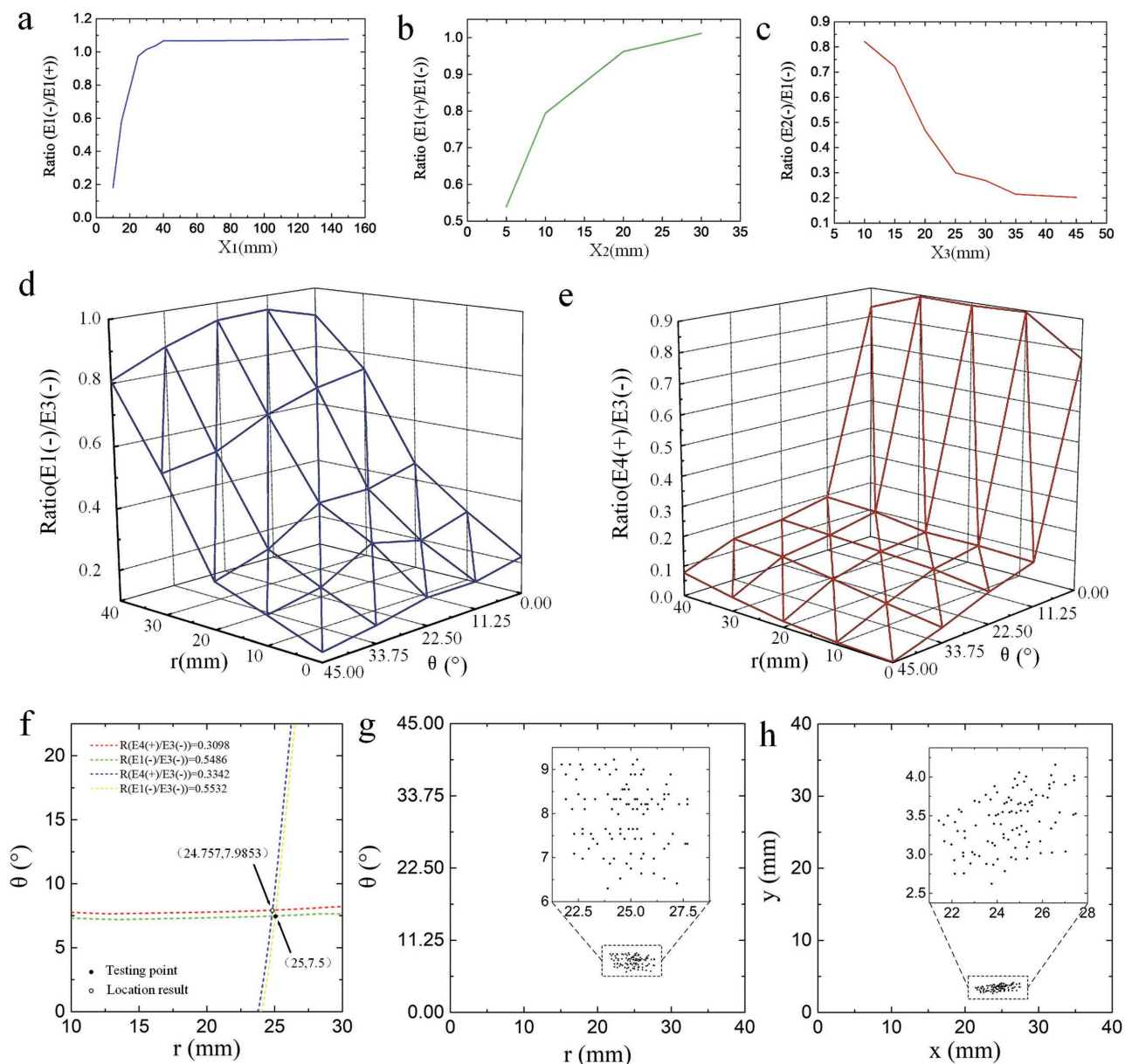
Figure 4. Testing results of double electrode and four electrodes electronic skin. An interpolation in R_r and R_θ was employed to localize the voltage ratio. a) Effect of x_1 and d in the ratio of E1's negative peak voltage over its fixed positive peak voltage. b) Effect of x_2 and d in the ratio of E1's positive peak voltage over its fixed negative peak voltage. c) Effect of x_3 and d in the ratio of E2's negative peak voltage over E1's fixed negative peak voltage. d) Distribution of R_r in the polar coordinate system. e) Distribution of R_θ in polar coordinate system. f) Comparison between actual testing point and location result. g) Location result of 100 tests applied to (25 mm, 7.5°) in polar coordinate system. h) Location result of 100 tests applied to (25 mm, 7.5°) in rectangular coordinate system, which is (24.786 mm, 3.263 mm).

with the simulations despite some minor deviations. Among these deviations, a slight decrease in $R_{n_1p_1}$ of Figure 4a during $x_1 > 50$ mm and a slight increase in $R_{n_1p_1}$ of Figure 4b is observed. This is caused by electrostatic induction of secondary induced charges. In Figure 4a, the deviations from the simulation results are caused by a small decrease in the negative peak voltage of E1 that becomes notable when $x_1 > 50$ mm, because increasing x_1 leads to the increase of voltage on E2 and more secondary induced negative charge flow on E1 which weakens the total induced positive charge during the distance decrease between E1 and the object. This secondary effect actually promotes the stability of $R_{n_1p_1}$ and makes it better for normalization factor. Similarly, in Figure 4b, voltage change in E2 increases when x_3 decreases (see Figure 3d), and this results in more secondary induced negative charge flow in E1 which adds in total induced negative charge during the distance increase period of E1, and thus causes $R_{p_1n_1}$ to increase. In Figure 4c, deviation is not as clear as in Figure 4a,b.

Figure 4d,e shows the distribution of R_r and R_θ in polar coordinates system, with $d = 2.5$ mm and $x_1 = 50$ mm. All of the points showed in Figure 4a–e are tested 10 times and average values are taken as the final ones. In accordance with Figure 4c,b, respectively, R_r fits well with the simulation result while there is a slight increase in R_θ due to the same reason with $R_{p_1n_1}$ in Figure 4b. In this time, positive charge flow in E1 (V_{n_1}) adds to the negative charge flow in E4 (V_{p_4}), while reduces the positive charge flow in E3 (V_{n_3}). Increase in R_θ in fact enhanced the signal–noise ratio, as the value of positive voltage in E4 (V_{p_4}) is relatively small. Despite the deviations from simulation results, the distribution of R_r and R_θ is still in good monotonicity with r and θ which enables it to be effective and reliable.

100 repeated tests were applied on a specific point (25 mm, 7.5°) in order to verify the reliability and resolution of the electronic skin. Interpolation was made to the testing result of R_r and R_θ across $r \in (20$ mm, 30 mm) and $\theta \in (0°, 11.25°)$ in polar coordinate system to calculate the result locations of 100 tests. The Interpolation result is displayed in Figure S2a,b (Supporting Information). As can be seen from Figure 4f, the average position of the 100 tests is (24.757 mm, 7.9853°), with a deviation from the actual point of 0.343 mm in the r direction and 0.4853° in the θ direction. Converting to rectangular coordinate system, the absolute deviation is 0.4 mm, which shows excellent accuracy of the electronic skin. On the other hand, the standard deviation is 1.5 mm in the r direction and 0.76° in the θ direction. The absolute deviation is 1.54 mm. As a result, the resolution around the point (2.5 mm, 7.5°) is 1.54 mm, which is remarkable. Figure 4g shows the distribution of 100 testing results in polar coordinate system, and Figure 4h shows the results in rectangular coordinate system. As can be seen in Figure 4h, aggregation in θ direction is better than the r direction, because $|\frac{\partial R_\theta}{\partial \theta}| > |\frac{\partial R_r}{\partial r}|$ when $r = 2.5$ mm and $\theta = 7.5°$, and this leads to more accurate discrimination with the same voltage deviation. Resolution in θ direction may decrease when θ increases because $|\frac{\partial R_\theta}{\partial \theta}|$ and R_θ decreases with θ and thus causing the signal–noise ratio of the waveform of E4 as well as the discrimination accuracy to decrease, while both of them lead to the decrease in resolution. However, given

the high signal–noise ratio demonstrated in Figure 2b–d, and the smooth change in R_θ across the plane, the r-resolution is expected not to decrease observably.

Aside from theoretical results that the output of the electronic skin is irrelevant to the amount of charges and moving speed, 100 sets of data during the verification test were also obtained to prove this conclusion. Figure S2c,d (Supporting Information) displayed the irrelevance of charge density and moving speed with the location result. The absolute peak voltage is determined by both variables, while the FWHM is only related to moving speed. The discontinuity in FWHM is caused by the sampling frequency of the oscilloscope, which is 2.5 MHz. Clearly, the result in Figure S2c,d (Supporting Information) supported the theoretical claim.

Our electronic skin can serve as a human machine interface, since it allows users to send signals without contacting the interface, so that it provides more freedom and fun for them. The electronic skin as a control interface of a MATLAB based Tetris game is demonstrated in **Figure 5**. Figure 5a shows the game platform which contains an oscilloscope with four probes, a laptop computer, a router, two cables, and the electronic skin. The electronic skin was attached to the screen of the computer right above the game window, and the four electrodes were connected to the probes of the oscilloscope. A 2 cm × 2 cm microstructured PDMS film was attached to a finger-cot wore by the researcher, who plays the game with a distance between his index finger and the screen of 1–2 cm. Figure 5b demonstrated the data flow chart, and realization of the game platform can be found in the Experimental Section. Four kinds of interaction waveforms with high signal–noise ratio were displayed in Figure 5c, which are shaking movements of a finger above and across the four electrodes respectively. In Video S1 (Supporting Information), three movements across the left, right, and top electrodes were displayed. The whole platform was shown first and then the scene focused onto the game window and the electronic skin. The electronic skin converts the movements into electric signals through electrostatic induction effect which can be transmitted, processed, and responded quickly with a frequency ≈1 Hz. This shows that our electronic skin is practical in realizing a real-time fast-response human machine interface capable of various tasks like game control interfaces. A novel approach in human machine interaction, featuring noncontact interactions that provide amusement and unique experiences for the users, is successfully developed; thus showing a broad perspective in potential applications. In addition, our smart skin is obviously feasible for more kinds of inputs, e.g., simultaneously moving the thumb and the index finger above two opposite electrodes, as well as vertical movements.

3. Conclusion

In conclusion, our flexible, transparent, and self-powered noncontact electronic skin provides a new approach for noncontact motion sensing, with a resolution up to 1.5 mm and a distance deviation of 0.4 mm, which shows excellent accuracy and can be further enhanced due to its theoretical infinite resolution. The main novelties of this work compared with previous ones
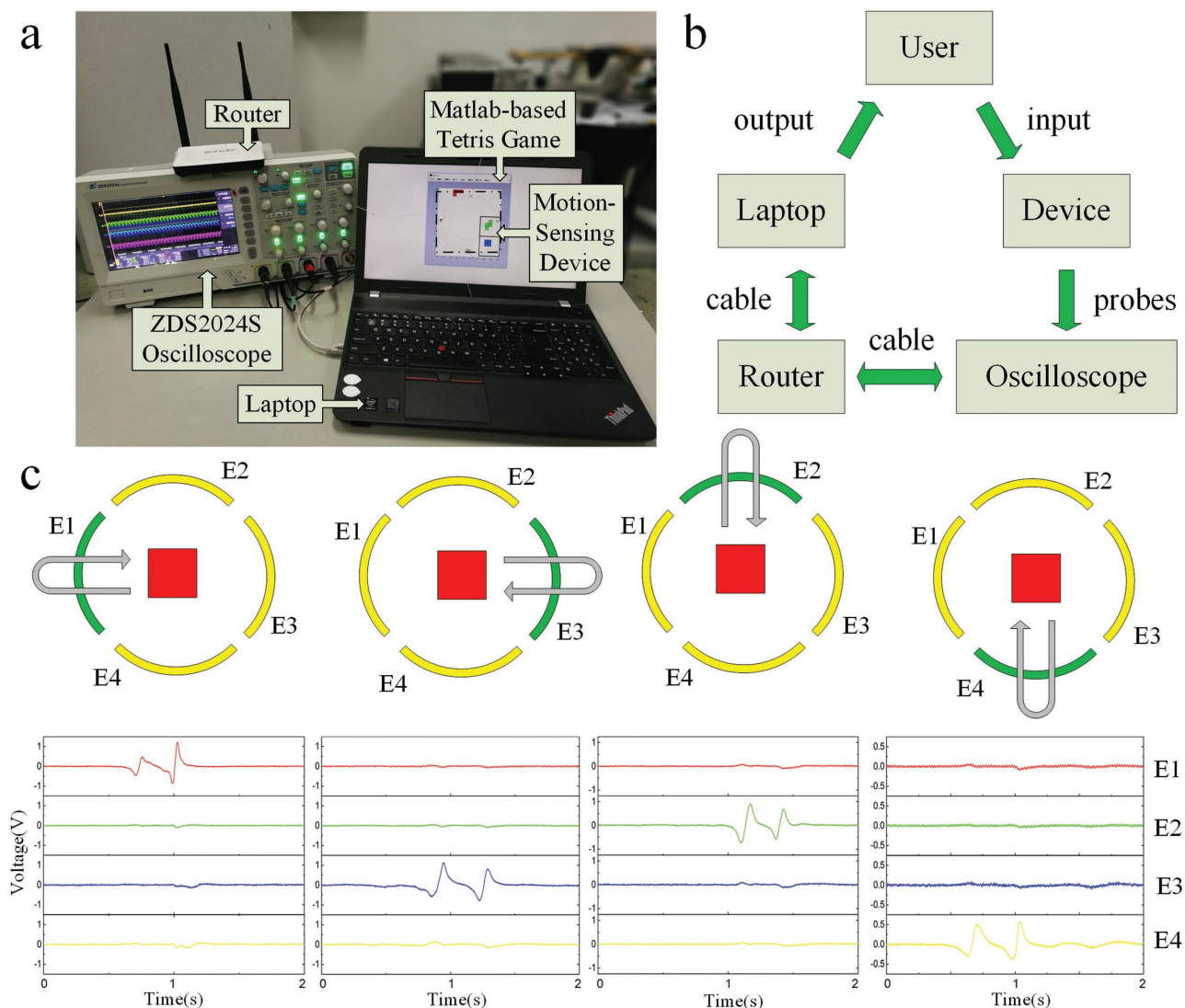
Figure 5. Application of noncontact electronic skin as a real-time human machine interface. a) Scene of the Tetris game platform consisting of an oscilloscope with four probes, a laptop computer, a router connecting the oscilloscope and the computer with two cables, and the electronic skin for motion sensing. b) Data flow chart of the system. c) Waveforms of four different motions captured by the oscilloscope and recognized by the MATLAB script, which corresponds to shaking patterns above and across the left, right, top, and bottom electrodes.

are that this device extended the field of motion sensing into noncontact mode, and we designed novel configurations of electrodes catering the motion sensing under polar coordinates; in addition, we derived theoretical calculation approaches based on the working mechanism and physical fundamentals, which is verified by simulation and experimental results. The trilayer of PET–ITO–PDMS determined the flexible and transparent characteristic of the electronic skin as well as excellent durability and reliability. The self-powering feature is enabled by triboelectric effects, which harness the energy in the motion itself. Spatial electrostatic induction allows users to have versatile inputs compared with traditional contact localizing methods. A real-time game platform with the electronic skin serving as the control interface is realized, proving its feasibility in practical application. Therefore, the results demonstrated here paved the way for the noncontact electronic skin

to become new generation of human machine interface, with a promising future in applications for artificial intelligence.

4. Experimental Section

Fabrication of Si Mold: (100) orientation Si wafer with thermally grown SiO_2 was prepared. Lithography was used to pattern square window arrays (10 µm length and 10 µm gap between each other) on the SiO_2 layer. Then reactive ion etching process was performed to etch out the SiO_2 with SF_6 and expose the silicon surface. Residual photoresist was cleaned with acetone. The SiO_2 with square window arrays serves as the hard mask, and KOH solution (together with isopropyl and deionized water) etching was applied. The Si mold with pyramid structures was prepared.

Fabrication of the Microstructured PDMS Film: Elastomer and the cross-linker (Sylgard 184, Dow Corning) were prepared in the ratio 10:1 (w/w). The mixture was put on the Si mold for 30 min to wait for its

self-leveling. Then it was heated at 80 °C for 2 h. Remove the PDMS film from the Si mold carefully and the film is microstructured.

Setup of the MATLAB Based Tetris Game Platform: A LabVIEW script in the computer controls the setup and data flow of the ZDS2024S oscilloscope through wired Transmission Control Protocol/Internet Protocol (TCPIP) connections via a router to the computer while data processing and game interface are launched by a MATLAB script. The interval of the game was set to be 1 s, but delay exists due to data transmission and processing. The overall data-catching rate (length of time during which waveform is captured over the total time in an interval) exceeds 70%, and this occasionally causes some minor malfunctions which can be seen in Video S1 (Supporting Information).

Supporting Information

Supporting Information is available from the Wiley Online Library or from the author.

Conflict of Interest

The authors declare no conflict of interest.

[1] M. L. Hammock, A. Chortos, B. C. Tee, J. B. Tok, Z. Bao, *Adv. Mater.* **2013**, *25*, 5997.

[2] X. Wang, L. Dong, H. Zhang, R. Yu, C. Pan, Z. L. Wang, *Adv. Sci. (Weinheim, Ger.)* **2015**, *2*, 1500169.

[3] S. Park, H. Kim, M. Vosgueritchian, S. Cheon, H. Kim, J. H. Koo, T. R. Kim, S. Lee, G. Schwartz, H. Chang, Z. Bao, *Adv. Mater.* **2014**, *26*, 7324.

[4] C. Wang, D. Hwang, Z. Yu, K. Takei, J. Park, T. Chen, B. Ma, A. Javey, *Nat. Mater.* **2013**, *12*, 899.

[5] S. El-Molla, A. Albrecht, E. Cagatay, P. Mittendorfer, G. Cheng, P. Lugli, J. F. Salmerón, A. Rivadeneyra, *J. Sens.* **2016**, *1*, 1606151.

[6] Y.-C. Lai, B.-W. Ye, C.-F. Lu, C.-T. Chen, M.-H. Jao, W.-F. Su, W.-Y. Hung, T.-Y. Lin, Y.-F. Chen, *Adv. Funct. Mater.* **2016**, *26*, 1286.

[7] Z. Lou, S. Chen, L. Wang, K. Jiang, G. Shen, *Nano Energy* **2016**, *23*, 7.

[8] W. Yang, J. Chen, X. Wen, Q. Jing, J. Yang, Y. Su, G. Zhu, W. Wu, Z. L. Wang, *ACS Appl. Mater. Interfaces* **2014**, *6*, 7479.

[9] H. Chen, Z. Su, Y. Song, X. Cheng, X. Chen, B. Meng, Z. Song, D. Chen, H. Zhang, *Adv. Funct. Mater.* **2017**, *27*, 1604434.

[10] C. Pang, G. Y. Lee, T. I. Kim, S. M. Kim, H. N. Kim, S. H. Ahn, K. Y. Suh, *Nat. Mater.* **2012**, *11*, 795.

[11] D. H. Ho, Q. Sun, S. Y. Kim, J. T. Han, D. H. Kim, J. H. Cho, *Adv. Mater.* **2016**, *28*, 2601.

[12] S. Zhao, R. Zhu, *Adv. Mater.* **2017**, *29*, 1736169.

[13] L. Cai, L. Song, P. Luan, Q. Zhang, N. Zhang, Q. Gao, D. Zhao, X. Zhang, M. Tu, F. Yang, W. Zhou, Q. Fan, J. Luo, W. Zhou, P. M. Ajayan, S. Xie, *Sci. Rep.* **2013**, *3*, 3048.

[14] M. Shi, H. Wu, J. Zhang, M. Han, B. Meng, H. Zhang, *Nano Energy* **2017**, *32*, 479.

[15] M. L. Hammock, A. N. Sokolov, R. M. Stoltenberg, B. D. Naab, Z. Bao, *ACS Nano* **2012**, *6*, 3100.

[16] W. Zhong, Q. Liu, Y. Wu, Y. Wang, X. Qing, M. Li, K. Liu, W. Wang, D. Wang, *Nanoscale* **2016**, *8*, 12105.

[17] M. Park, Y. J. Park, X. Chen, Y. K. Park, M. S. Kim, J. H. Ahn, *Adv. Mater.* **2016**, *28*, 2556.

[18] M. S. Sarwar, Y. Dobashi, C. Preston, J. K. M. Wyss, S. Mirabbasi, J. D. W. Madden, *Sci. Adv.* **2017**, *3*, 1602200.

[19] U. Khan, T. H. Kim, H. Ryu, W. Seung, S. W. Kim, *Adv. Mater.* **2017**, *29*, 1603544.

[20] T. Sekitani, T. Someya, *MRS Bull.* **2012**, *37*, 236.

[21] Q. Sun, W. Seung, B. J. Kim, S. Seo, S. W. Kim, J. H. Cho, *Adv. Mater.* **2015**, *27*, 3411.

[22] Q. Wang, M. Jian, C. Wang, Y. Zhang, *Adv. Funct. Mater.* **2017**, *27*, 1605657.

[23] M. Ma, Z. Zhang, Q. Liao, F. Yi, L. Han, G. Zhang, S. Liu, X. Liao, Y. Zhang, *Nano Energy* **2017**, *32*, 389.

[24] K. Hu, R. Xiong, H. Guo, R. Ma, S. Zhang, Z. L. Wang, V. V. Tsukruk, *Adv. Mater.* **2016**, *28*, 3549.

[25] W. Deng, L. Jin, B. Zhang, Y. Chen, L. Mao, H. Zhang, W. Yang, *Nanoscale* **2016**, *8*, 16302.

[26] X. Cheng, B. Meng, X. Zhang, M. Han, Z. Su, H. Zhang, *Nano Energy* **2015**, *12*, 19.

[27] X. Chen, Y. Song, Z. Su, H. Chen, X. Cheng, J. Zhang, M. Han, H. Zhang, *Nano Energy* **2017**, *38*, 43.

[28] B. Meng, W. Tang, Z.-h. Too, X. Zhang, M. Han, W. Liu, H. Zhang, *Energy Environ. Sci.* **2013**, *6*, 3235.

[29] X. S. Zhang, M. D. Han, R. X. Wang, F. Y. Zhu, Z. H. Li, W. Wang, H. X. Zhang, *Nano Lett.* **2013**, *13*, 1168.

[30] M. Chen, X. Li, L. Lin, W. Du, X. Han, J. Zhu, C. Pan, Z. L. Wang, *Adv. Funct. Mater.* **2014**, *24*, 5059.

[31] X. Y. Li, J. A. Tao, W. X. Guo, X. J. Zhang, J. J. Luo, M. X. Chen, J. Zhu, C. F. Pan, *J. Mater. Chem. A* **2015**, *3*, 22663.

[32] M. Shi, J. Zhang, H. Chen, M. Han, S. A. Shankaregowda, Z. Su, B. Meng, X. Cheng, H. Zhang, *ACS Nano* **2016**, *10*, 4083.

[33] F. Visentin, P. Fiorini, K. Suzuki, *Sensors (Basel)* **2016**, *16*, 1928.

[34] X. S. Zhang, M. D. Han, R. X. Wang, F. Y. Zhu, Z. H. Li, W. Wang, H. X. Zhang, *Nano Lett.* **2013**, *13*, 1168.